Aalborg Universitet

Analysis of High-Frequency Resonance in DFIG-based Offshore Wind Farm via Long Transmission Cable

Song, Yipeng; Ebrahimzadeh, Esmaeil; Blaabjerg, Frede

Published in:
I E E E Transactions on Energy Conversion

DOI (link to publication from Publisher):
10.1109/TEC.2018.2794367

Publication date:
2018

Document Version
Accepted author manuscript, peer reviewed version

Link to publication from Aalborg University

Citation for published version (APA):
Song, Y., Ebrahimzadeh, E., & Blaabjerg, F. (2018). Analysis of High-Frequency Resonance in DFIG-based Offshore Wind Farm via Long Transmission Cable. *I E E E Transactions on Energy Conversion*, *33*(3), 1036 - 1046. Article 8259448. https://doi.org/10.1109/TEC.2018.2794367

General rights
Copyright and moral rights for the publications made accessible in the public portal are retained by the authors and/or other copyright owners and it is a condition of accessing publications that users recognise and abide by the legal requirements associated with these rights.

- Users may download and print one copy of any publication from the public portal for the purpose of private study or research.
- You may not further distribute the material or use it for any profit-making activity or commercial gain
- You may freely distribute the URL identifying the publication in the public portal -

Take down policy
If you believe that this document breaches copyright please contact us at vbn@aub.aau.dk providing details, and we will remove access to the work immediately and investigate your claim.

Downloaded from vbn.aau.dk on: June 18, 2025

This article has been accepted for publication in a future issue of this journal, but has not been fully edited. Content may change prior to final publication. Citation information: DOI 10.1109/TEC.2018.2794367, IEEE Transactions on Energy Conversion

Analysis of High Frequency Resonance in DFIG-based Offshore Wind Farm via Long Transmission Cable

Yipeng Song, *Member, IEEE*, Esmaeil Ebrahimzadeh, *Student Member,* Frede Blaabjerg, *Fellow, IEEE*

***Abstract* — During the past two decades, the Doubly Fed Induction Generator (DFIG) based wind farm has been under rapid growth, and the increasing wind power penetration has been seen. Practically, these wind farms are connected to the three-phase AC grid through long transmission cable which can be modelled as several Π units. The impedance of this cable cannot be neglected and requires careful investigation due to its long distance. As a result, the impedance interaction between the DFIG based wind farm and the long cable is inevitable, and may produce High Frequency Resonance (HFR) in the wind farm. This paper discusses the HFR of the large scale DFIG based wind farm connected to the long cable. Several influencing factors, including 1) the length of the cable, 2) the output active power and 3) the rotor speed, are investigated. The transformer leakage inductances in the transmission system are taken into consideration when investigating the HFR. Simulation validations using MATLAB / Simulink have been conducted to verify the theoretical analysis.**

***Index Terms* — DFIG system; wind farm; Π unit model based long transmission cable; high frequency resonance; transformer leakage inductance.**

I. INTRODUCTION

During the past two decades, the Doubly Fed Induction Generator (DFIG) based wind farm has been under rapid growth and contributes to the increasing penetration of wind power. As the wind power generation techniques develop, several wind power plant configurations are implemented, including the High Voltage Direct Current (HVDC) based offshore wind farm and the High Voltage Alternating Current (HVAC) based offshore wind farm [1]-[3]. Improved control strategies for DFIG based wind power system considering grid voltage fault [4], virtual inertia control [5], grid voltage unbalance [6]-[7], grid voltage harmonic distortion [8] as well as connection to the dc voltage grid [9] have been investigated.

As a common commercial solution, the DFIG based HVAC offshore wind farm is to be discussed in this paper, with two characters of 1) the multiple DFIG units in the wind farm are working in parallel through a common AC bus connection at the voltage level of 33 / 66 kV; 2) the offshore location requires long transmission cables at the voltage level of 150 kV, thus its impedance is relatively large and can not be neglected.

As investigated in previous works [10]-[12], the impedance modeling of the long transmission cable is in this paper assumed to be a series connection of several Π units, which contain a cable resistance and cable inductance in series connection and cable shunt capacitance between the cable and the ground at both ends [10]-[12].

On the other hand, the DFIG based wind power system consists of the DFIG generator and the Rotor Side Converter (RSC), as well as the Grid Side Converter (GSC) with the output LCL filter. Since the DFIG system behaves mostly inductive in the control frequency range [12]-[15], the DFIG based wind farm with hundreds of DFIG units will also behave inductive under these circumstances.

Due to the inductive behavior of the DFIG based wind farm and the capacitive behavior of the long transmission cable, a resonance may happen as a consequence of the impedance interaction in certain frequency range. Note that the High Frequency Resonance (HFR) has been investigated in [12]-[15], and the corresponding active damping strategies for the HFR were proposed in [12]-[13], [15]. However, only a single DFIG system, rather than a wind farm with multiple DFIGs in parallel connections, was discussed. Furthermore, no detailed discussion on the impedance modeling of the long transmission cable was given.

Compared with the previous studies [12]-[15], the main contribution of this paper is the HFR in DFIG based wind farm containing large numbers of DFIG units, as well as the long transmission cables. Besides, several influencing factors on the HFR, including 1) the length of the cable, 2) the output active power and 3) the rotor speed, will be studied. Moreover, the leakage inductance of the voltage-level increasing transformer in the wind farm may always exist in the practice, thus the transformer leakage inductance needs to be taken into consideration when discussing the HFR.

It is essential to point out that besides the HFR to be discussed in this paper, the DFIG based wind farm is also likely to suffer Sub-Synchronous Resonance (SSR) which has been under investigation for decades [16]-[22]. One major difference between the SSR and HFR is that the SSR always happens at the frequency below the fundamental frequency, while the HFR is always much higher than the fundamental frequency. The other difference is that these two resonances happen under different conditions, i.e., the SSR occurs under the condition of the series compensated transmission cable with intentionally inserted series capacitance, while the HFR occurs under the condition of the shunt capacitance connected to the transmission cable. Therefore, it can be seen that these two resonances are independent resonance phenomena, and the main topic of this paper is the HFR in the wind farm connected to the long transmission cable.

0885-8969 (c) 2017 IEEE. Personal use is permitted, but republication/redistribution requires IEEE permission. See http://www.ieee.org/publications_standards/publications/rights/index.html for more information.

This paper is organized as following: the impedance modeling of a single DFIG system unit will be discussed as an analysis platform, then the impedance modeling of the overall DFIG based wind farm can be obtained in Section II. Thereafter, the impedance modeling of the long transmission cable at 150 kV AC bus is established in Section III. Then, the HFR can be analyzed on the basis of the obtained impedance modeling of both the wind farm and the transmission cable which is described in Section IV. Finally, the simulation validations based on MATLAB / Simulink are provided in Section V in order to verify the analysis of the HFR in the DFIG based wind farm.

II. IMPEDANCE MODELING OF WIND FARM AND TRANSMISSION CABLES

Before establishing the impedance modeling, it is firstly necessary to introduce the configuration of the DFIG based wind farm and the long transmission cables as shown in Fig. 1. It needs to be pointed out that the HFR discussed in this paper is above the frequency of 1 kHz. While, the synchronization closed-loop control bandwidth is typically below 100 Hz [4]-[5], and the output power closed-loop control bandwidth is also typically below 100 Hz [4]-[5]. Thus, the synchronization and power control loop can be neglected when investigating the HFR.

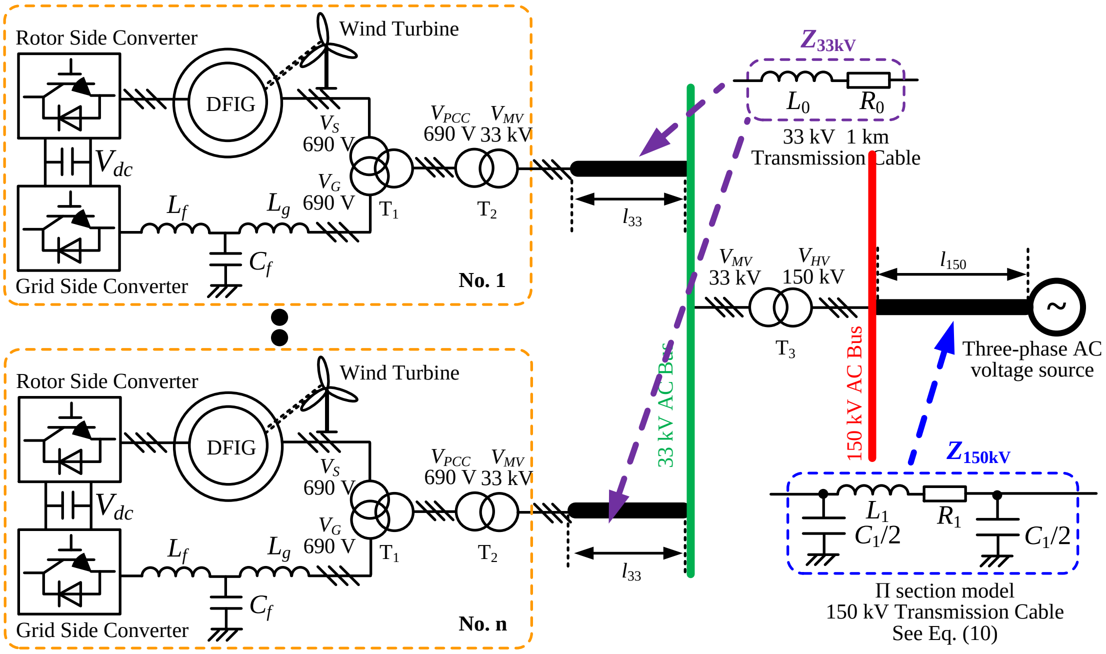

Fig. 1. Diagram of the DFIG based wind farm with n wind turbines connected to a long transmission cable

A. *Introduction to the wind farm and long cable*

Fig. 1 shows the diagram of the DFIG based wind farm connected to the long transmission cable. For each of the single DFIG unit, it contains two parts, i.e., 1) the RSC and the DFIG generator, 2) the GSC and the output LCL filter. The output voltages of these two parts are adjusted through a three-terminal transformer T_1 to be 690 V. The parameters of the DFIG system unit are shown in Table I.

Then, in order to connect each single DFIG unit to the 33 kV AC bus, the transformer T_2 is adopted to increase the voltage level from 690 V to 33 kV. The short transmission cable at 33 kV is used to connect between the output of each unit and the 33 kV common bus. Since the length of the 33 kV cable is relatively short set as 1 km [23], it is modelled as a series connection of cable resistor R_0 and a cable inductor L_0. Multiple DFIG units together build up the large scale DFIG based wind farm with a common connection to a 33 kV AC bus.

After collecting the wind power at 33 kV AC bus, the voltage level is again increased up to 150 kV through the transformer T_3. The long transmission cable at 150 kV is assumed to be much longer than the 33 kV cable, and it is modelled as the series connection of several Π units, i.e., the cable resistor R_1 and the cable inductor L_1 in series connection and the cable shunt capacitor $C_1/2$ between the cable and the ground at both ends.

TABLE I. PARAMETERS OF 2 MW DFIG UNITS AND LONG TRANSMISSION CABLES

DFIG generator			
Rated Power	2 MW	T_d	300 μs
R_s	0.0015 Ω	R_r	0.0016 Ω
$L_{\sigma s}$	0.04 mH	$L_{\sigma r}$	0.06 mH
L_m	3 mH	Pole Pairs	3
f_s	5 kHz	f_{sw}	2.5 kHz
LCL filter			
L_g	125 μH	L_f	125 μH
C_f	220 μF		
Current Controller Parameters in RSC and GSC			
K_{prsc}	0.08	K_{irsc}	2
K_{pgsc}	0.08	K_{igsc}	2
Voltage level			
V_G	690 V	V_{SR}	690 V
V_{PCC}	690 V	V_{MV}	33 kV
V_{HV}	150 kV		
Transmission cable			
L_0	0.4 mH/km	R_0	70 mΩ/km
C_0	0.14 μF/km		

0885-8969 (c) 2017 IEEE. Personal use is permitted, but republication/redistribution requires IEEE permission. See http://www.ieee.org/publications_standards/publications/rights/index.html for more information.

B. *Impedance modeling of the DFIG based wind farm*

The impedance modeling of the single DFIG unit is established first in this section. Note that the impedance modeling of the single DFIG unit, including both the RSC and the DFIG generator, as well as the GSC and the output LCL filter, has been obtained as done in [12]-[15]. Here for the sake of simplicity, the impedances of the two parts are mentioned here as the following.

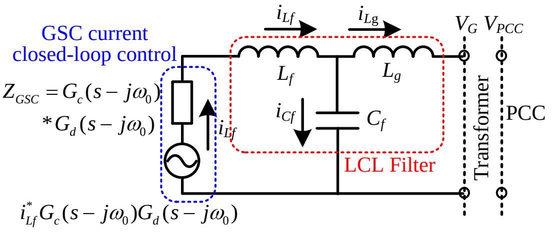

Fig. 2. Impedance modeling of the Grid Side Converter (GSC) equipped with LCL filter.

The grid part of the DFIG system contains the GSC and the LCL filter, and its impedance modeling [12]-[15] in the stationary frame is presented in Fig. 2. Then, the impedance of the DFIG grid side in the stationary frame can be obtained as,

$$Z_G=K_1^2\frac{Z_{Cf}\left(Z_{Lf}+Z_{GSC}\right)+Z_{Lg}\left(Z_{Lf}+Z_{GSC}\right)+Z_{Cf}Z_{Lg}}{Z_{Cf}+\left(Z_{Lf}+Z_{GSC}\right)} \quad (1)$$

where, $Z_{Cf}=1/sC_f$, $Z_{Lf}=sL_f$, $Z_{Lg}=sL_g$. C_f is the LCL-filter capacitance, L_f is the converter side inductance, and L_g is the LCL grid side inductance. K_1 is the voltage ratio between V_G and V_{PCC} defined as $K_1=V_{PCC}/V_G$. $Z_{GSC}=G_c(s\text{-}j\omega_0)G_d(s\text{-}j\omega_0)$, $G_c(s\text{-}j\omega_0)$ is the PI current controller containing the proportional part K_{pgsc} and the integral part $K_{igsc}/(s\text{-}j\omega_0)$, the parameters of K_{pgsc} and K_{igsc} can also be found in Table I. $G_d(s\text{-}j\omega_0)$ is the digital control delay of 1.5 sample period due to the delay of sampling and PWM update [12]-[15]. It needs to be pointed out that ω_0 is the grid fundamental component angular speed of 100π rad/s. The introduction of ω_0 is due to the reference frame rotation from the stationary frame to the synchronous frame, where the PI closed-loop current control is implemented. The control loop of the dc-link voltage and the grid synchronization in the GSC are neglected due to the slower dynamic response [12]-[15].

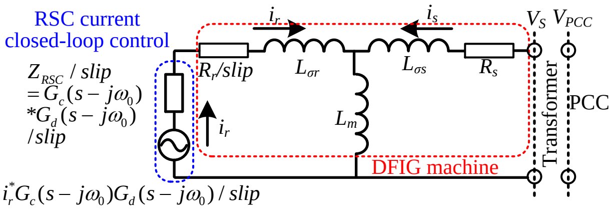

Fig. 3. Impedance modeling of the DFIG generator and Rotor Side Converter (RSC).

On the other hand, the impedance of the RSC and DFIG generator [12]-[15] in the stationary frame can be obtained in Fig. 3 as,

$$Z_{SR}=K_2^2\frac{Z_{Lm}H+\left(R_s+Z_{L\sigma s}\right)H+Z_{Lm}\left(R_s+Z_{L\sigma s}\right)}{Z_{Lm}+H} \quad (2)$$

where $H=Z_{L\sigma r}+(R_r+Z_{RSC})/slip$; $Z_{RSC}=G_c(s\text{-}j\omega_0)G_d(s\text{-}j\omega_0)$, $Z_{Lm}=sL_m$; $Z_{L\sigma r}=sL_{\sigma r}$; $Z_{L\sigma s}=sL_{\sigma s}$. R_r is the rotor resistance, L_m is the mutual inductance, $L_{\sigma r}$ is the rotor leakage inductance, and $L_{\sigma s}$ is the stator leakage inductance. K_2 is the voltage ratio between V_S and V_{PCC} as defined $K_2=V_{PCC}/V_S$. Since the rotor current control is implemented in the synchronous reference frame, it needs to be transformed into the rotor stationary frame using the slip angular speed expressed as [12]-[15],

$$slip=\left(s-j\omega_r\right)/s \quad (3)$$

where, ω_r is the rotor angular speed.

Since the RSC and DFIG generator Z_{SR} and the GSC and LCL-filter Z_G are connected in parallel, the single DFIG unit impedance Z_{single} can be obtained based on (1) and (2) as,

$$Z_{single}=K_3^2\frac{Z_GZ_{SR}}{Z_G+Z_{SR}} \quad (4)$$

where, $K_3=V_{MV}/V_{PCC}$.

Based on the impedance modeling of the single DFIG unit shown above, two conclusions can be obtained,

1) The impedance modeling of the single DFIG unit does not involve its output power, which indicates that different output power is irrelevant to the impedance of the DFIG unit;

2) The variable rotor speed does not cause any significant variation of the rotor slip value in the high frequency range, which indicates that the rotor speed is also irrelevant to the impedance of the DFIG unit.

Based on the above two conclusions, it is appropriate and reasonable to assume that all the DFIG units in the wind farm are working in the same condition in parallel, thus the impedance of the entire wind farm can be obtained by dividing the impedance of the single DFIG unit with the number of units n, while at the same time taking into consideration the 33 kV cable.

$$Z_{farm}=\frac{1}{n}\left(Z_{single}+sl_{33}L_0+l_{33}R_0\right) \quad (5)$$

where, n is the number of DFIG units, l_{33} is the length of the 33 kV cable, L_0 and R_0 is the resistance and inductance per km of the 33 kV cable given in Table I.

Importantly, it needs to be pointed out that, from the engineering perspective, the current control bandwidth using PI controller is normally selected as 1/20 – 1/10 of the switching frequency $f_{sw}=2.5$ kHz for the sake of satisfactory closed-loop control performance [25], that is, 125 Hz – 250 Hz for the current closed-loop control in the DFIG based wind farm discussed in this paper. On the other hand, the HFR is comparatively at much higher frequency range above 1 kHz. Therefore, based on above explanation, it is believed that the current control bandwidth in RSC and GSC (which is from 125 Hz to 250 Hz) and the HFR (which is above 1 kHz) are indeed irrelevant to each other.

C. *Impedance modeling of the long transmission cable*

The modeling of the transmission cable has been well investigated in [24] and the Π unit based cable modeling is a common solution which is shown in Fig. 4.

0885-8969 (c) 2017 IEEE. Personal use is permitted, but republication/redistribution requires IEEE permission. See http://www.ieee.org/publications_standards/publications/rights/index.html for more information.

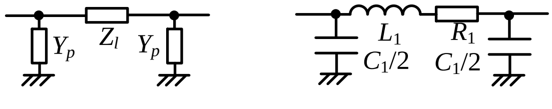

(a) (b)

Fig. 4. Π unit based modeling of the long transmission cable (a) accurate modeling; (b) simplified modeling.

On one hand, the accurate Π unit based cable modeling shown in Fig. 4(a) can be calculated as the following [24],

$$Z_l = Z_c \sinh(\gamma l) \tag{6}$$

$$Y_p = (\cosh(\gamma l) - 1) / (Z_c \sinh(\gamma l)) \tag{7}$$

where, l is the length of the cable; Z_c and γ are the surge impedance and the propagation constant of the cable respectively, which can be expressed as,

$$Z_c = \sqrt{\frac{L_0}{C_0}} - j\frac{1}{2}\frac{R_0}{\omega\sqrt{L_0 C_0}} \tag{8}$$

$$\gamma = \frac{R_0}{2}\sqrt{\frac{C_0}{L_0}} + j\omega\sqrt{L_0 C_0} \tag{9}$$

where, R_0, C_0 and L_0 are the cable resistance, capacitance and inductance per km given in Table I.

On the other hand, considering that the accurate modeling in Fig. 4(a) is mathematically complicated for the analysis in this paper, it is necessary to adopt the simplified Π unit based cable modeling as shown in Fig. 4(b). As it can be seen, the simplified Π unit contains the cable resistance R_1 and inductance L_1 in series connection, and the shunt capacitance $C_1/2$ between the cable and the ground. Note that R_1, L_1 and C_1 are the cable parameters of each single Π unit, and the length of each single Π unit l_{single} needs to be taken into consideration.

$$R_1 = l_{\text{single}} R_0; L_1 = l_{\text{single}} L_0; C_1 = l_{\text{single}} C_0; \tag{10}$$

Then, based on the above assumptions, the simplified Π unit based cable modeling can be deduced as following,

1) One PI unit and its impedance expression $Z_{\text{unit(1)}}$

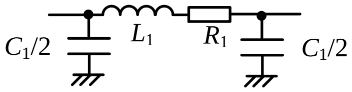

$$Y_{unit(1)} = \frac{1}{sL_1 + R_1} + \frac{sC_1}{2};\ Z_{unit(1)} = \frac{1}{K_4^2 Y_{unit(1)}} \tag{11a}$$

2) Two PI units and its impedance expression $Z_{\text{unit(2)}}$

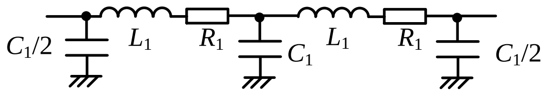

$$Y_{unit(2)} = \frac{1}{sL_1 + R_1 + \frac{1}{\frac{1}{sL_1 + R_1} + sC_1}} + \frac{sC_1}{2} = \frac{1}{sL_1 + R_1 + \frac{1}{Y_{unit(1)} + \frac{sC_1}{2}}} + \frac{sC_1}{2};\ Z_{unit(2)} = \frac{1}{K_4^2 Y_{unit(2)}} \tag{11b}$$

3) Three PI units and its impedance expression Zunit(3)

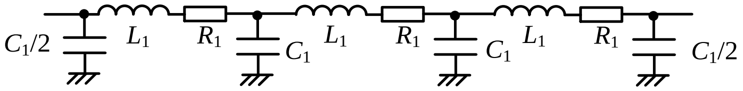

$$Y_{unit(3)} = \frac{1}{sL_1 + R_1 + \frac{1}{Y_{unit(2)} + \frac{sC_1}{2}}} + \frac{sC_1}{2};\ Z_{unit(3)} = \frac{1}{K_4^2 Y_{unit(3)}} \tag{11c}$$

4) Based on above deduction, it can be seen that the cable impedance expression is a kind of iteration, therefore the impedance of the n PI units can be deduced on the basis of the n-1 PI units.

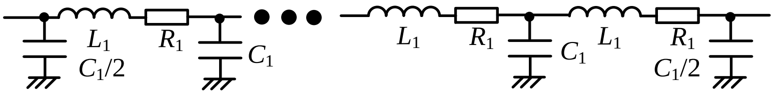

$$Y_{unit(n)} = \frac{1}{sL_1 + R_1 + \frac{1}{Y_{unit(n-1)} + \frac{sC_1}{2}}} + \frac{sC_1}{2};\ Z_{unit(n)} = \frac{1}{K_4^2 Y_{unit(n)}} \tag{11d}$$

where, $K_4 = V_{HV}/V_{MV}$ is the voltage ratio between the high voltage V_{HV} = 150 kV and the medium voltage V_{MV} = 33 kV.

D. Comparison between the accurate and the simplified cable modeling

In order to verify that the simplified model in Fig. 4(b) is sufficiently accurate to represent the accurate model given in Fig. 4(a), these two models need to be compared in the interested frequency range.

As it can be found from (6) - (11), the length of the single unit l_{single} and the number of Π units n can vary during the modeling (while the total cable length l can be calculated as $l = l_{single} * n$). The following discussions are conducted using different single unit lengths l_{single} = 2, 3, 4 km per unit and the unit number n = 12, 8, 6 correspondingly, thus the total length l is set constant as 24 km.

As shown in Fig. 5(a), the best accuracy of the simplified modeling among the three cases can be achieved with the shortest single unit length l_{single} = 2 km. However the largest

0885-8969 (c) 2017 IEEE. Personal use is permitted, but republication/redistribution requires IEEE permission. See http://www.ieee.org/publications_standards/publications/rights/index.html for more information.

This article has been accepted for publication in a future issue of this journal, but has not been fully edited. Content may change prior to final publication. Citation information: DOI 10.1109/TEC.2018.2794367, IEEE Transactions on Energy Conversion

number $n = 12$ is required with the highest complexity. On the contrary, when the unit length increases as $l_{single} = 3$ km in Fig. 5(b) and $l_{single} = 4$ km in Fig. 5(c), the modeling accuracy decreases, but the modeling becomes simpler with less Π units.

By comparing the three cases in Fig. 5, it can be seen that the shorter length of the single unit ensures better cable modeling accuracy, however at the expense of higher cable modeling complexity. From the perspective of compromise between the modeling accuracy and complexity, the length of a single unit is chosen as $l_{single} = 3$ km per unit in the following discussion.

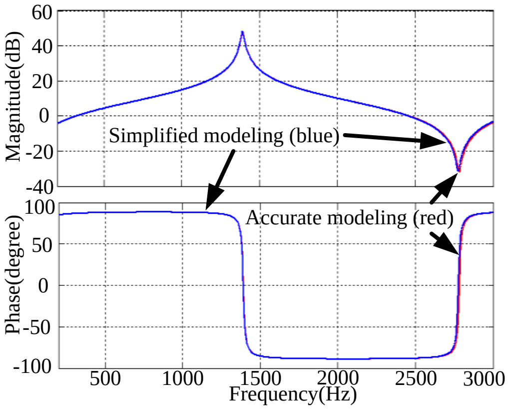

(a) $l_{single} = 2$ km per unit; the unit number $n = 12$

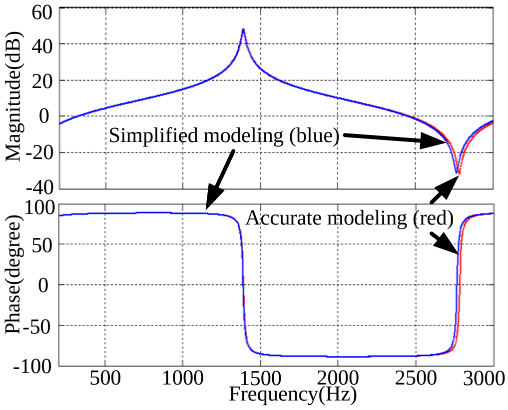

(b) $l_{single} = 3$ km per unit; the unit number $n = 8$

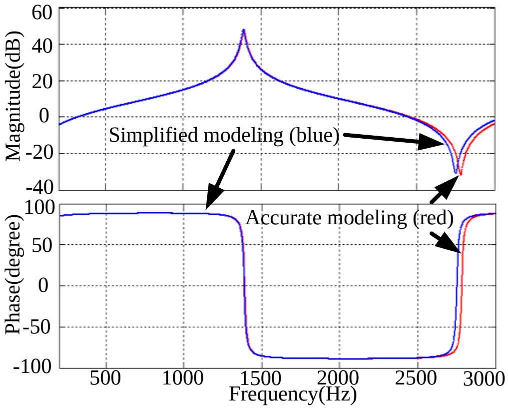

(c) $l_{single} = 4$ km per unit; the unit number $n = 6$

Fig. 5. Bode diagram of the accurate modeling (red) and simplified modeling (blue) of the transmission cable (a) $l_{single} = 2$ km per unit; the unit number $n = 12$; (b) $l_{single} = 3$ km per unit; the unit number $n = 8$; (c) $l_{single} = 4$ km per unit; the unit number $n = 6$;

III. ANALYSIS OF HFR IN WIND FARM

Based on the impedance modeling obtained in the above section, the HFR can be analyzed using the Bode diagram analysis method.

A. *Discussion regarding different lengths of 150 kV cable*

The impedance interaction between the DFIG based wind farm and the long transmission cable can be investigated at the point of the 33 kV AC bus. Note that, three cases of different total cable lengths will be discussed in the following analysis, i.e., total length $l = 18$ km (with 6 Π units), 24 km (with 8 Π units), 30 km (with 10 Π units). The rated power of each single DFIG unit is set as 2 MW, and it is assumed that 200 DFIG units are working together in the wind farm, thus building up the total capacity of 400 MW.

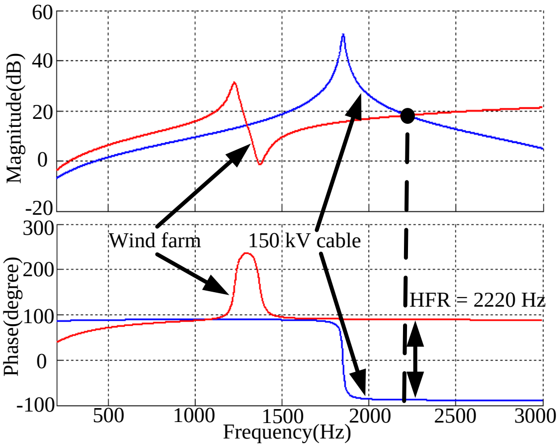

(a) Wind farm: 200 DFIG units, total capacity of 400 MW; 150 kV Cable: 6 π units, 18 km

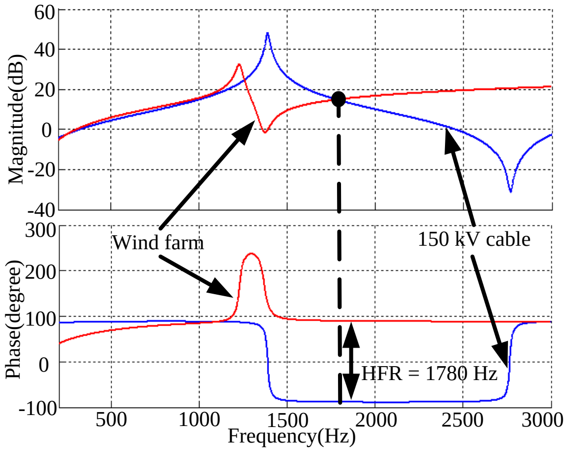

(b) Wind farm: 200 DFIG units, total capacity of 400 MW; 150 kV Cable: 8 π units, 24 km

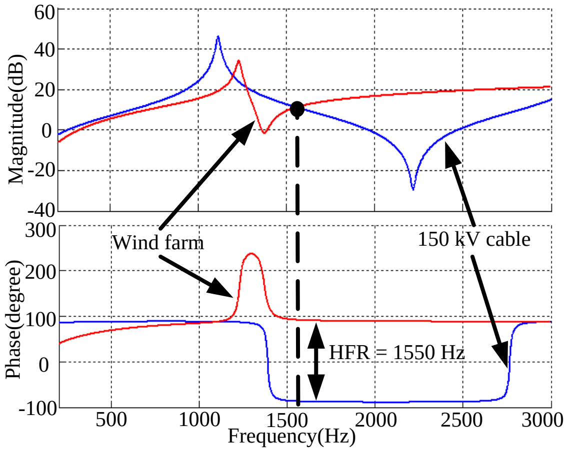

(c) Wind farm: 200 DFIG units, total capacity of 400 MW; 150 kV Cable: 10

0885-8969 (c) 2017 IEEE. Personal use is permitted, but republication/redistribution requires IEEE permission. See http://www.ieee.org/publications_standards/publications/rights/index.html for more information.

π units, 30 km

Fig. 6. Bode diagram of the impedance of the 400 MW DFIG based wind farm and the impedance of the 150 kV transmission cable with (a) 150 kV cable: 6 Π units, 18 km; (b) 150 kV cable: 8 Π units, 24 km; (c) 150 kV cable: 10 Π units, 30 km. Parameters are shown in Table I.

Fig. 6 shows the Bode diagram of the impedance of the 400 MW DFIG based wind farm and the impedance of the 150 kV transmission cable with (a) 150 kV cable: 6 Π units, 18 km; (b) 150 kV cable: 8 Π units, 24 km; (c) 150 kV cable: 10 Π units, 30 km. The parameters of the DFIG unit and 150 kV transmission cable are listed in Table I. The length of the 33 kV cable is set as 1 km.

As it can be seen from Fig. 6(a), the impedance of the 6 Π units 18 km 150 kV transmission cable in blue has one magnitude peaks in the interested frequency range, and its phase response varies between +90° and -90°. On the other hand, the wind farm behaves mostly inductive with a phase response of +90°. As shown in Fig. 6(a), the magnitude intersection point exists between the wind farm and the long cable at 2220 Hz, and the phase difference at this frequency is 180°, therefore the HFR consequently occurs at 2220 Hz.

Similarly, for the case of 150 kV cable with 8 Π units, 24 km shown in Fig. 6(b), the magnitude intersection point between the wind farm and the long cable at 1780 Hz has a phase difference of 180°, thus causing the HFR at 1780 Hz as a result.

Moreover, for the case of 150 kV cable using 10 Π units, 30 km as shown in Fig. 6(c), the magnitude intersection point at 1550 Hz has the phase difference of 180° between the wind farm and the long cable, which indicates the occurrence of the HFR at 1550 Hz.

It should be noted that for all the three cases discussed in Fig. 6, there are additional magnitude intersection points in the Bode diagrams, however the phase difference at these intersection points are smaller than 180°, therefore the potential HFR maybe well damped at these frequencies due to the sufficient damping.

Based on the above discussions regarding different length of the 150 kV transmission cable with different numbers of Π units, it can be seen that the occurrence of the HFR in the wind farm depends partly on the length of the transmission cable, or to be more specific, on the impedance behavior of the transmission cable.

Furthermore, it can be seen that the frequency of the HFR tends to become lower due to the magnitude peak shifting towards lower frequency range as the transmission cable becomes longer.

B. *Discussion regarding different rotor speed and output power*

Besides the different cable length discussed above, the rotor speed is also a variable in practice, it is meaningful to discuss the influence of the rotor speed on the occurrence of the HFR.

However, based on the impedance modeling of the single DFIG unit Z_{single}, it can be observed that the rotor speed is irrelevant to its impedance modeling. Thus, the rotor speed is not important to the occurrence of HFR in the wind farm. This conclusion will be validated by some simulation results shown in the following.

Similarly, the output wind power is not included in the impedance modeling of the single DFIG either. As a consequence, the output wind power is not important to the occurrence of HFR, which will also be verified in the following simulation results.

IV. SIMULATION VALIDATION

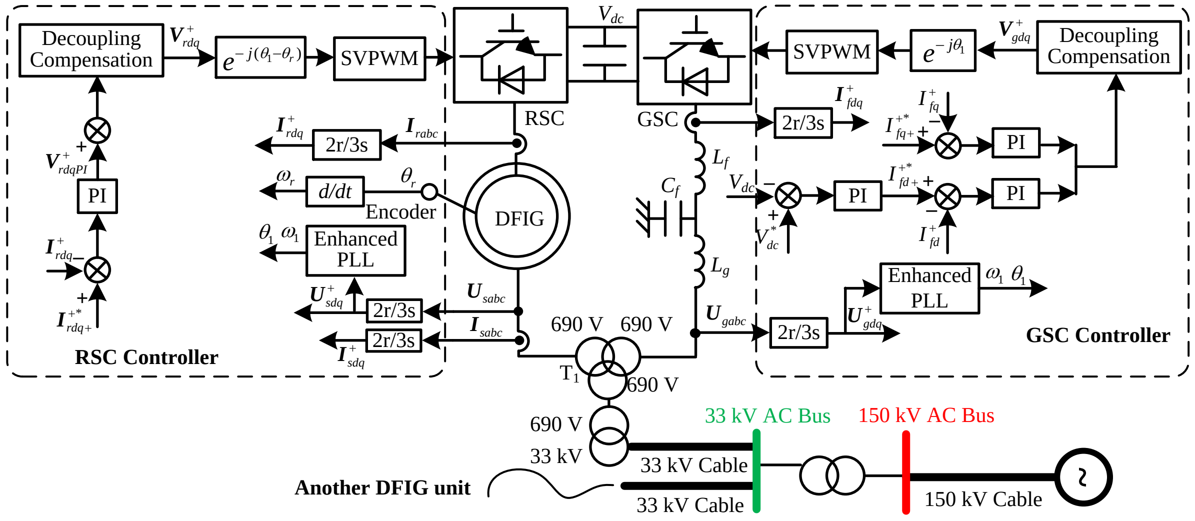

Fig. 7. Control block diagram of a single DFIG unit including the connection to the grid through long transmission cables

A. *Simulation setup*

In order to validate the HFR in the wind farm, a simulation model is built up, the control block is shown in Fig. 7, and the DFIG system parameters can be found in Table I. The transmission cables are simulated as shown in Fig. 1 with their parameters listed in Table I. The rotor speed is set to 1200 rpm (0.8 p.u.), with the synchronous speed of 1500 rpm (1.0 p.u.). The dc-link voltage is 1200 V. The switching frequency f_{sw} for both RSC and GSC is 2.5 kHz, the sampling frequency f_s for both RSC and GSC is 5 kHz. The output wind power is set as 1.0 p.u. active power and 0.0 p.u. reactive power.

Since it is impossible to run the simulation based on MABLAB/Simulink with 200 single DFIG units, two single

0885-8969 (c) 2017 IEEE. Personal use is permitted, but republication/redistribution requires IEEE permission. See http://www.ieee.org/publications_standards/publications/rights/index.html for more information.

DFIG units are adopted here, while the impedance of the transmission cables are multiplied with 100 to represent the total number of 200 DFIG units, which finally build up a 400 MW wind farm.

B. Control block diagram

Fig. 7 shows the control block diagram of a single DFIG unit including the connection to the grid through long transmission cables. As it can be seen, for the RSC control, an Enhanced Phase Locked Loop (EPLL) is used to provide the information of grid voltage fundamental synchronous angular speed ω_1 and angle θ_1 information, while an encoder gives out the DFIG rotor position θ_r and speed ω_r. The rotor current $\boldsymbol{I}_{rdq}^{+}$ is first sampled and then controlled based on the reference value $\boldsymbol{I}_{rdq}^{+*}$ with a PI controller to output the harvested wind energy. The output of the rotor current PI closed-loop control $\boldsymbol{V}_{rdqPI}^{+}$ are added together with the decoupling compensation, giving out the rotor control voltage $\boldsymbol{V}_{rdq}^{+}$, which is then transformed to the rotor stationary frame and delivered as the input to the Space Vector Pulse Width Modulation (SVPWM).

As for the GSC control, the dc-link voltage V_{dc} is well regulated by a PI controller, and its output is delivered as the converter side inductance filter current reference $\boldsymbol{I}_{fdq}^{+*}$, which is used to regulate the actual converter side inductance filter current $\boldsymbol{I}_{fdq}^{+}$ by a PI controller. Similarly, the GSC control voltage $\boldsymbol{V}_{gdq}^{+}$ can be obtained by the PI current controller output and the decoupling compensation.

C. Steady state simulation results

Fig. 8 – Fig. 10 show the steady state simulation results of the DFIG waveforms with three cases of different 150 kV cable length, that is, 6 Π units, 18 km in Fig. 8; 8 Π units, 24 km in Fig. 9; 10 Π units, 30 km in Fig. 10.

As it can be observed from Fig. 8 – Fig. 10, the DFIG waveforms of all the three cases contain high frequency resonance components. By comparing the simulation results in Fig. 8 – Fig. 10 with the theoretical analysis in Fig. 6, it can be seen that the simulation results match well with the theoretical analysis, that is,

1) Analysis HFR = 2220 Hz in Fig. 6(a) and simulation HFR = 2245 Hz in Fig. 8(b) for the case of 150 kV cable using 6 Π units, 18 km;

2) Analysis HFR = 1780 Hz in Fig. 6(b) and simulation HFR = 1800 Hz in Fig. 9(b) for the case of 150 kV cable using 8 Π units, 24 km;

3) Analysis HFR = 1550 Hz in Fig. 6(c) and simulation HFR = 1575 Hz in Fig. 10(b) for the case of 150 kV cable using 10 Π units, 30 km.

Thus, the steady state simulation results are able to validate the analysis of the HFR in the wind farm.

D. Simulation results with variable rotor speed and variable output power

Fig. 11 shows the simulation results of DFIG waveform when the output power steps from 1.0 p.u. to 0.5 p.u. and the 150 kV cable is modelled as 10 Π units, 30 km. It can be observed that the HFR remains constant both before and after the output power is changed. Thus, it can be verified that the output power of the DFIG based wind farm is irrelevant to the HFR phenomenon.

Fig. 12 shows the simulation results of DFIG waveform when the rotor speed is 1.2 p.u. and the 150 kV cable is modelled as 10 Π units, 30 km. By comparing Fig. 10 and Fig. 12, it can be seen that the HFR phenomenon of these two simulation results are the same, thus it can be verified that the rotor speed is not important to the HFR in the DFIG based wind farm.

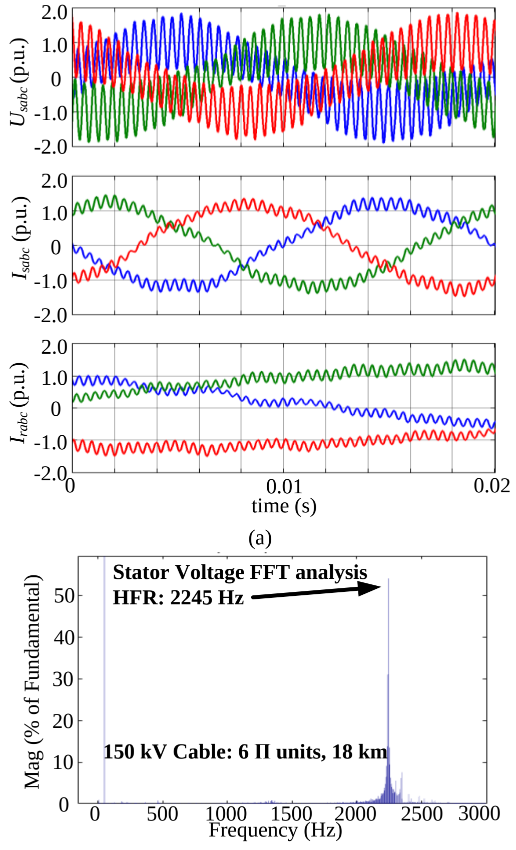

(a)

(b)

Fig. 8. Simulation results of DFIG waveform when the cable using 6 Π units, 18 km. (a) system performance; (b) stator voltage FFT analysis

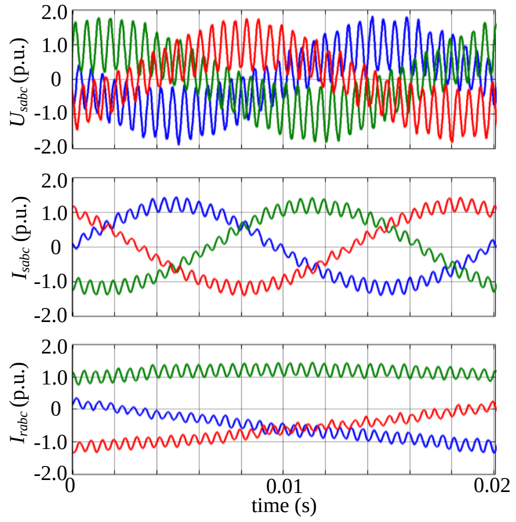

(a)

0885-8969 (c) 2017 IEEE. Personal use is permitted, but republication/redistribution requires IEEE permission. See http://www.ieee.org/publications_standards/publications/rights/index.html for more information.

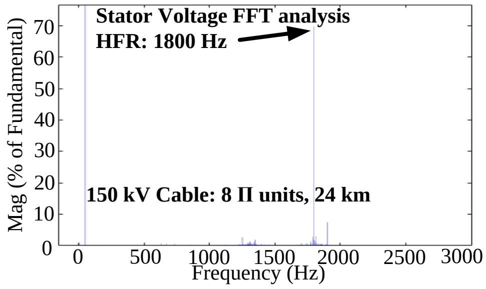

(b)

Fig. 9. Simulation results of DFIG waveform when the cable using 8 Π units, 24 km. (a) system performance; (b) stator voltage FFT analysis

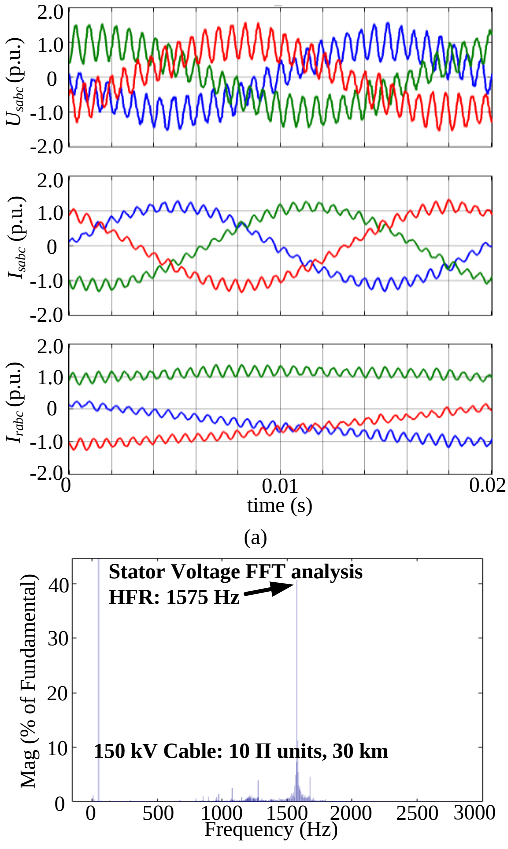

(a)

(b)

Fig. 10. Simulation results of DFIG waveform when the cable using 10 Π units, 30 km. (a) system performance; (b) stator voltage FFT analysis

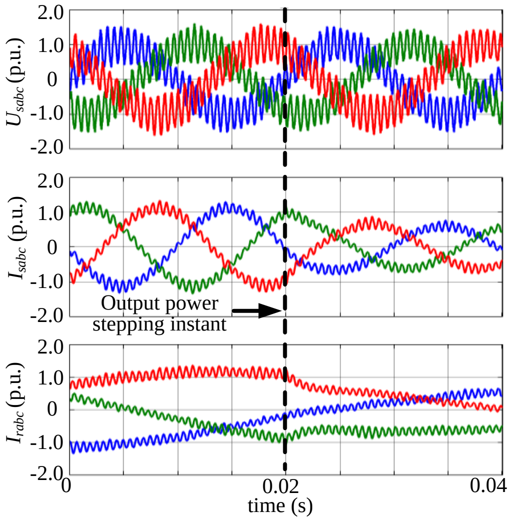

(a)

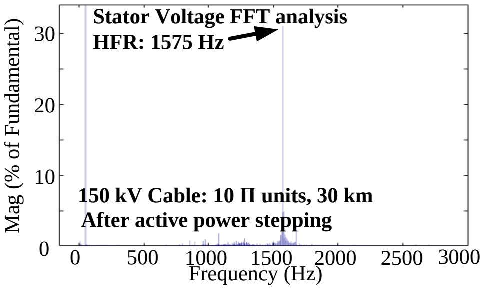

(b)

Fig. 11. Simulation results of DFIG waveform when the output power steps from 1.0 p.u. to 0.5 p.u. and the cable using 10 Π units, 30 km. (a) system performance; (b) stator voltage FFT analysis

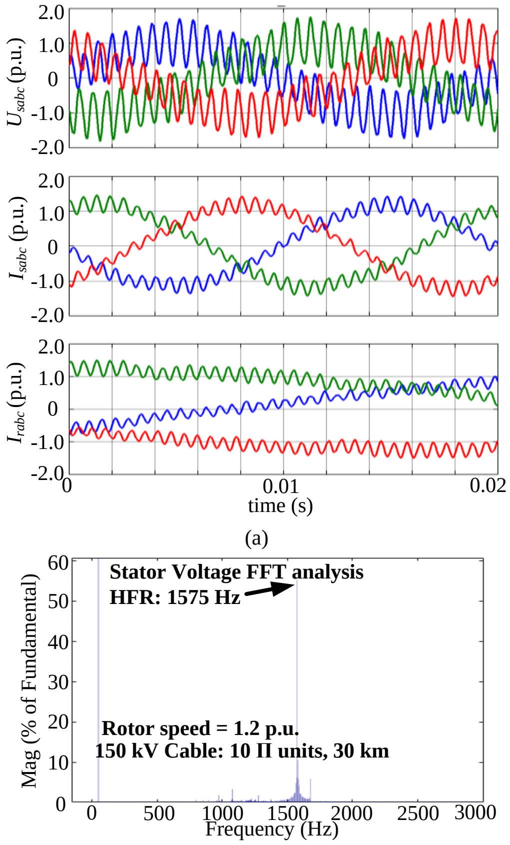

(a)

(b)

Fig. 12. Simulation results of DFIG waveform when the rotor speed is 1.2 p.u. and the cable using 10 Π units, 30 km. (a) system performance; (b) stator voltage FFT analysis

V. DISCUSSION ON THE INFLUENCE OF TRANSFORMER LEAKAGE INDUCTANCE ON HFR

It should be pointed out that the HFR analysis above is conducted under the assumption that the transformer is ideal without the consideration of the leakage inductance at both low and high voltage side windings. However, if the leakage inductance of the transformer is considerable against the inductance of the filter, it should be taken into consideration. The following part discusses the HFR performance when the different transformer leakage inductances is included during the impedance modeling, and the transformer of 690 V / 33 kV shown as T2 in Fig. 1 is taken as an example. Three different case studies will be conducted as following.

0885-8969 (c) 2017 IEEE. Personal use is permitted, but republication/redistribution requires IEEE permission. See http://www.ieee.org/publications_standards/publications/rights/index.html for more information.

TABLE II. THREE CASE STUDIES OF LEAKAGE INDUCTANCE

Leakage inductance	at low voltage side 690 V	at high voltage side 33 kV
Case I	15 μH	34 mH
Case II	38 μH	86 mH
Case III	76 μH	173 mH

TABLE III. COMPARISON BETWEEN THEORETICAL ANALYSIS AND SIMULATION REGARDING LEAKAGE INDUCTANCE

	Theoretical analysis in Fig. 13	Simulations in Fig. 14 to 16
Case I	1660 Hz	1670 Hz
Case II	1570 Hz	1575 Hz
Case III	1510 Hz	1500 Hz

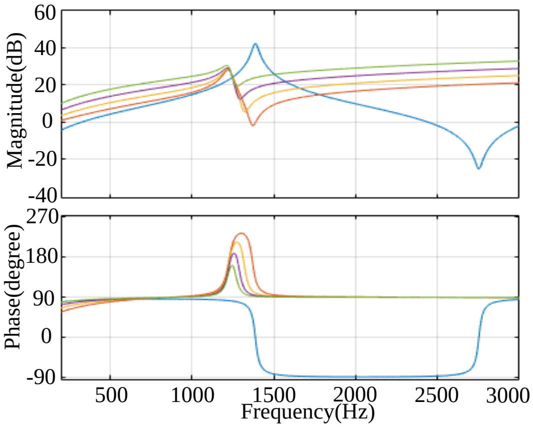

Fig. 13. The impedance bode diagram of the cable (in blue), the DFIG system without leakage inductance (in red), Case I (in yellow), Case II (in purple), Case III (in green).

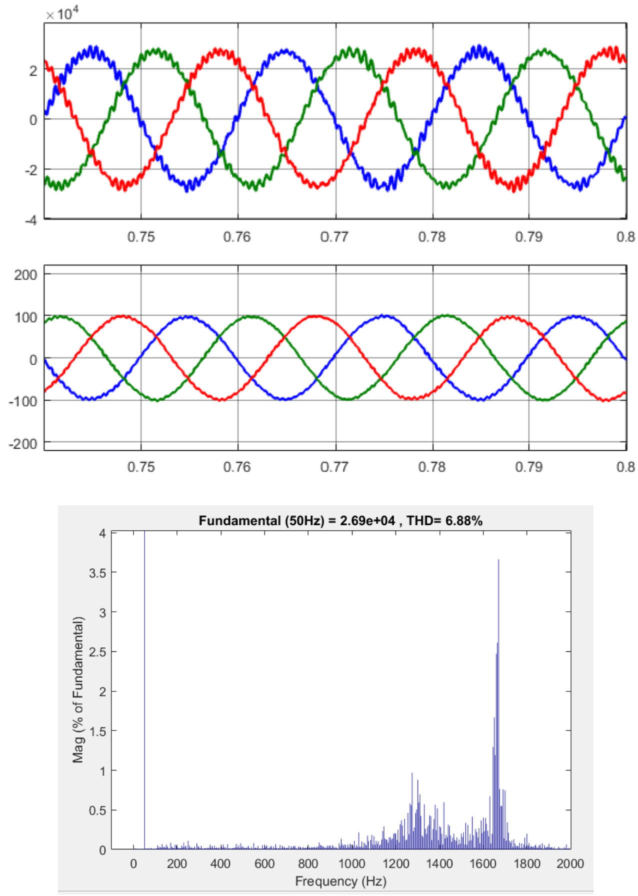

Fig. 14. Simulation results of 33 kV AC bus voltage (upper) and current (lower) for Case I, and the FFT analysis of the 33 kV AC bus voltage (1670 Hz)

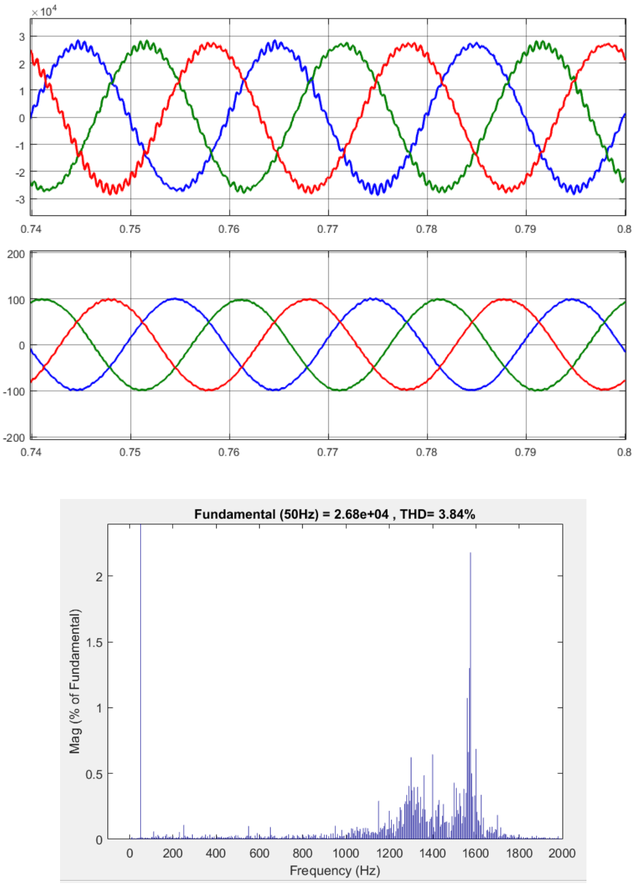

Fig. 15. Simulation results of 33 kV AC bus voltage (upper) and current (lower), for Case II, and the FFT analysis of the 33 kV AC bus voltage (1575 Hz)

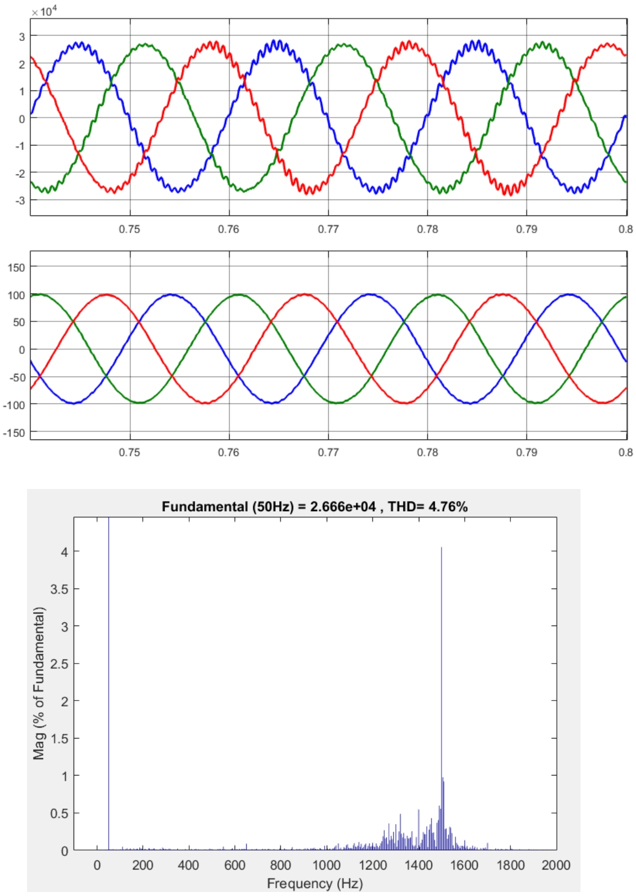

0885-8969 (c) 2017 IEEE. Personal use is permitted, but republication/redistribution requires IEEE permission. See http://www.ieee.org/publications_standards/publications/rights/index.html for more information.

This article has been accepted for publication in a future issue of this journal, but has not been fully edited. Content may change prior to final publication. Citation information: DOI 10.1109/TEC.2018.2794367, IEEE Transactions on Energy Conversion

Fig. 16. Simulation results of 33 kV AC bus voltage (upper) and current (lower) for Case III, and the FFT analysis of the 33 kV AC bus voltage (1500 Hz)

The Bode diagram of the impedances is shown in Fig. 13, including different leakage inductances of the transformer. As it can be seen from Fig. 13, when the transformer leakage inductance becomes larger, the impedance curve of the DFIG system goes higher, and the magnitude intersection point between the cable and the DFIG system shifts towards lower frequency direction from 1780 Hz to 1660 Hz, 1570 Hz and 1510 Hz. In order to validate the theoretical analysis above, the time domain simulations of four different case studies are conducted, and the simulation results are shown in Fig. 14 - 16.

Thus, it can be found out that the time domain simulation results match well with the Bode diagram based theoretical analysis results, and the methodology used to identify the HFR in this paper is verified again with the inclusion of the different transformer leakage inductances.

VI. CONCLUSION

This paper has investigated the HFR phenomenon in the DFIG based wind farm connected to the long transmission cables, which are modelled as several Π units, i.e., the cable resistor and inductor in series connection and the shunt capacitor at both ends between the cable and the ground. Several conclusions can be drawn.

1) The Bode diagram based analysis method can be adopted to theoretically explain the principle of the HFR, and simulation results are provided to validate the HFR.

2) The longer transmission cable results in more Π units, and consequently a lower HFR frequency due to the magnitude peak shifting towards lower frequency range as the transmission cable becomes longer.

3) The variable rotor speed and the output wind power are irrelevant to the wind farm HFR phenomenon since these two elements are not involved in the impedance modeling of the DFIG system.

It is also important to note that the HFR discussed here is typically above 1 kHz, therefore the skin effect may have certain influence. However, "how serious this influence is" may vary and be dependent on the different cable manufacture materials. Thus, for the sake of simplicity, the skin effect is not taken into consideration, and maybe an interesting topic in the future. Furthermore, the analysis of the contribution factors of the several DFIG system components on the resonance could definitely be an interesting topic to investigate in the future works.

REFERENCES

[1] F. Blaabjerg, and K. Ma, "Future on Power Electronics for Wind Turbine Systems," *IEEE J. Emer. Sel. Topics Power Electron.*, vol. 1, no. 3, pp. 139-152, Sep. 2013.

[2] K. Ma, L. Tutelea, I. Boldea, D. M. Ionel, F. Blaabjerg, "Power Electronic Drives, Controls, and Electric Generators for Large Wind Turbines–An Overview", *Electric Power Components and Systems*, vol. 43, no. 12, pp. 1406-1421, 2015.

[3] V. Yaramasu, B. Wu, P. C. Sen, S. Kouro, and M. Narimani, "High-power wind energy conversion systems: State-of-the-art and emerging technologies," *Proceedings of the IEEE*, vol. 103, no. 5, pp. 740 – 788, 2015.

[4] J. Hu, B. Wang, W. Wang, H. Tang, Y. Chi, Q. Hu. "Small Signal Dynamics of DFIG-based Wind Turbines during Riding Through Symmetrical Faults in Weak AC Grid," *IEEE Trans. Energy Convers*., accepted & in press.

[5] J. Hu, L. Sun, X. Yuan, S. Wang, Y. Chi. "Modeling of Type 3 Wind Turbine with df/dt Inertia Control for System Frequency Response Study," *IEEE Trans. Power Systems*, accepted & in press.

[6] H. Nian, P. Cheng, and Z. Q. Zhu, "Independent Operation of DFIG-Based WECS Using Resonant Feedback Compensators Under Unbalanced Grid Voltage Conditions," *IEEE Trans. Power Electron.*, vol. 30, no. 7, pp. 3650 - 3661, July 2015.

[7] H. Nian, P. Cheng, and Z. Q. Zhu, "Coordinated Direct Power Control of DFIG System Without Phase-Locked Loop Under Unbalanced Grid Voltage Conditions," *IEEE Trans. Power Electron.*, vol. 31, no. 4, pp. 2905 - 2918, April 2016.

[8] C. Wu, H. Nian, "Stator Harmonic Currents Suppression for DFIG Based on Feed-forward Regulator Under Distorted Grid Voltage," *IEEE Trans. Power Electron*., accepted.

[9] H. Nian, C. Wu, P. Cheng, "Direct Resonant Control Strategy for Torque Ripple Mitigation of DFIG Connected to DC Link through Diode Rectifier on Stator," *IEEE Trans. Power Electron*., accepted.

[10] M. Zubiaga, G. Abad, J.A. Barrena, S. Aurtenetxea, A. Cárcar, "Spectral analysis of a transmission system based on AC submarine cables for an offshore wind farm," *in Proc. of Annual Conference of IEEE Industrial Electronics* (IECON), Nov. 3-5, 2009.

[11] H. Zhang, G. François, F. Diana, S. Christophe, "Analysis of the influence of different cable modelling for DC series offshore wind farm," *in Proc. of Power Electronics and Applications* (EPE'16 ECCE Europe), Sept. 5-9, 2016.

[12] Y. Song, F. Blaabjerg, X. Wang, "Analysis and Active Damping of Multiple High Frequency Resonances in DFIG System," *IEEE Trans. Energy Convers.*, vol. 32, no. 1, pp. 369–381, March 2017.

[13] Y. Song, X. Wang, F. Blaabjerg, "High Frequency Resonance Damping of DFIG based Wind Power System under Weak Network," *IEEE Trans. Power Electron*., vol. 32, no. 3, pp. 1927-1940, March 2017.

[14] Y. Song, X. Wang, F. Blaabjerg, "Impedance-Based High Frequency Resonance Analysis of DFIG System in Weak Grids," *IEEE Trans. Power Electron*., vol. 32, no. 5, pp. 3536-3548, May 2017.

[15] Y. Song, F. Blaabjerg, "Wide Frequency Band Active Damping Strategy for DFIG System High Frequency Resonance," *IEEE Trans. Energy., Convers.*, vol. 31, no. 4, pp. 1665-1675, Dec. 2016.

[16] I. Vieto, and J. Sun, "Damping of Subsynchronous Resonance Involving Type-III Wind Turbines," *in Proc. Control and Modeling for Power Electronics* (COMPEL), pp. 1-8, 2015.

[17] I. Vieto, and J. Sun, "Small-Signal Impedance Modeling of Type-III Wind Turbine," *in Proc. Power & Energy Society General Meeting* (PESG), pp. 1-5, 2015.

[18] I. Vieto, and J. Sun, "Real-time Simulation of Subsynchronous Resonance in Type-III Wind Turbines," *in Proc. Control and Modeling for Power Electronics* (COMPEL), pp. 1-8, 2014

[19] Z. Miao, "Impedance-Model-Based SSR Analysis for Type 3 Wind Generator and Series-Compensated Network," *IEEE Trans. Energy Convers.*, vol. 27, no. 4, pp. 984–991, Dec. 2012.

[20] L. Piyasinghe, Z. Miao, J. Khazaei, and L. Fan, "Impedance Model-Based SSR Analysis for TCSC Compensated Type-3 Wind Energy Delivery Systems," *IEEE Trans. Sustainable Energy.*, vol. 6, no. 1, pp. 179–187, Jan. 2015.

[21] L. Fan, and Z. Miao, "Nyquist-Stability-Criterion-Based SSR Explanation for Type-3 Wind Generators," *IEEE Trans. Energy Convers.*, vol. 27, no. 3, pp. 807–809, Sep. 2012.

[22] L. Fan, and Z. Miao, "Mitigating SSR Using DFIG-Based Wind Generation," *IEEE Trans. Sustainable Energy.*, vol. 3, no. 3, pp. 349–358, July 2012.

[23] https://en.wikipedia.org/wiki/List_of_offshore_wind_farms_in_Denmark

[24] Z. Chen, A. Luo, H. Kuang, L. Zhou, Y. Chen, Y. Huang, "Harmonic resonance characteristics of large-scale distributed power plant in wideband frequency domain," Electric Power Systems Research, vol. 143, pp. 53-65, 2017.

0885-8969 (c) 2017 IEEE. Personal use is permitted, but republication/redistribution requires IEEE permission. See http://www.ieee.org/publications_standards/publications/rights/index.html for more information.

[25] D. Zhou, F. Blaabjerg, "Bandwidth oriented proportional-integral controller design for back-to-back power converters in DFIG wind turbine system," IET Renewable Power Generation, vol. 11, no. 7, pp. 941 – 951, June & July, 2017.

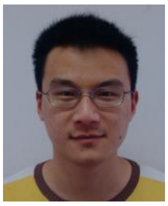

Yipeng Song (M'16) was born in Hangzhou, China. He received the B.Sc. degree and Ph.D. degree both from the College of Electrical Engineering, Zhejiang University, Hangzhou, China, in 2010 and 2015. He is currently working as a Postdoc at the Department of Energy Technology in Aalborg University, Denmark. His current research interests are motor control with power electronics devices in renewable-energy conversion, particularly the control and operation of doubly fed induction generators for wind power generation.

Esmaeil Ebrahimzadeh (S'16) received the M.Sc. degree in Electrical Engineering from University of Tehran, Tehran, Iran, where he has also been a lecturer for undergraduate Lab courses. Since 2015, he has employed as a PhD Fellow at the Department of Energy Technology, Aalborg University, Aalborg, Denmark. He has been a visiting R&D Engineer at Vestas Wind Systems A/S, Aarhus, Denmark, in 2017. His research interests include modeling, design, and control of power-electronic converters in different applications like renewable energy systems, and his main current project is focusing on power quality and stability analysis in large wind power plants. He is an IEEE student member and received the best paper awards at IEEE PEDG 2016 and IEEE PES GM 2017.

Frede Blaabjerg (S'86–M'88–SM'97–F'03) was with ABB-Scandia, Randers, Denmark, from 1987 to 1988. From 1988 to 1992, he was a Ph.D. Student with Aalborg University, Aalborg, Denmark. He became an Assistant Professor in 1992, Associate Professor in 1996, and Full Professor of power electronics and drives in 1998. His current research interests include power electronics and its applications such as in wind turbines, PV systems, reliability, harmonics and adjustable speed drives.

He has received 17 IEEE Prize Paper Awards, the IEEE PELS Distinguished Service Award in 2009, the EPE-PEMC Council Award in 2010, the IEEE William E. Newell Power Electronics Award 2014 and the Villum Kann Rasmussen Research Award 2014. He was an Editor-in-Chief of the IEEE TRANSACTIONS ON POWER ELECTRONICS from 2006 to 2012. He is nominated in 2014 and 2015 by Thomson Reuters to be between the most 250 cited researchers in Engineering in the world.

0885-8969 (c) 2017 IEEE. Personal use is permitted, but republication/redistribution requires IEEE permission. See http://www.ieee.org/publications_standards/publications/rights/index.html for more information.